EXPERIMENTAL ANALYSIS OF AN AXIAL COMPRESSOR OPERATING UNDER FLOW DISTORTION

Alberto Baretter[1] Pierric Joseph[1] Olivier Roussette[1] Francesco Romanó[1] Antoine Dazin[1]

[1]Univ. Lille, CNRS, ONERA, Arts et Metiers Institute of Technology, Centrale Lille Institut, UMR 9014-LMFL, Laboratoire de Mécanique des Fluides de Lille - Kampé de Fériet, F-59000, Lille, France.

ABSTRACT

In aircraft engines, compressor stages can encounter situations in which the flow is distorted at rotor inlet, for example during particular flight maneuvers, or due to the shape of the inlet of the airframe. The main objective of this paper is to investigate experimentally the effect of an inlet flow distortion on the internal flow dynamic and its consequences on the performance and operability of these machines. The distortion was generated by a porous plate grid installed upstream of the compressor. Eight total pressure rakes placed downstream of the grid were used to evaluate the distortion. Unsteady pressure measurements were performed on the casing at different axial and azimuthal positions to investigate the dynamic flow behavior at nominal conditions, at an operating point close to stall and during the transition to stall. 2D-2C PIV maps, synchronized with the runner position, were obtained on rotor blade-to-blade planes at three different spanwise positions (79%, 51%, 18% of the blade span). Three relative angular positions of the grid to the laser sheet were investigated at two different flow rates, namely the nominal flow rate and a flow rate close to stall. These three positions are corresponding to the laser sheet cutting through i/ the center of the grid's wake and ii/ the two edges of the grid. The impact of the distortion on the performance of the compressor is analyzed and compared to existing models. The impact of the flow dynamic will also be considered, especially in operations close to the stall limit.

Keywords: Inlet Distortion, Axial Compressor, Particle Image Velocimetry

NOMENCLATURE

b_x	Axial chord
P_t	Rakes relative total pressure
P_{s_u}	Rakes relative static pressure
P_{s_d}	Downstream relative static pressure
$P_{unsteady}$	Unsteady relative static pressure
r	Mean radius
T	Throttle loss coefficient
U	Blade speed at the mean radius
v_x	Axial component of velocity
λ	Inertial parameter in Hynes Greitzer model
Δp_{t-s}	Total to static pressure rise of the compressor stage
$\Delta\phi_* = \phi_{st\_exp} - \phi_{st\_*}$	Experimental-to-model flow coefficient deviation at stall conditions
$\Delta\psi_* = \psi_{st\_exp} - \psi_{st\_*}$	Experimental-to-model pressure coefficient deviation at stall conditions
γ	Stagger angle at mid radius
$\phi = v_x/U$	Flow coefficient
$\psi = \Delta p_{t-s}/(0.5\,\rho U^2)$	Pressure rise coefficient
$\psi_t = P_t/(0.5\,\rho U^2)$	Non dimensional rakes total pressure
$\psi_{s\_u} = P_{s\_u}/(0.5\,\rho U^2)$	Non dimensional rakes static pressure
$\psi_{s\_d} = P_{s\_d}/(0.5\,\rho U^2)$	Non dimensional downstream static pressure

Subscripts

pc	Parallel Compressor
HG	Hynes Greitzer
$*$	Either HG or pc
s	Static
st	Last stable point
t	Total

1. INTRODUCTION

In the last decade, the need to develop new ideas like boundary layer ingestion (BLI) to decrease fuel consumption in aircraft industry, has caused a revival in inlet distortion studies

[1,2,3,4]. The concept of BLI consists of taking advantage of the boundary layers developed on the fuselage of the aircraft to propel it [5]. It was already recognized in the 50s, during the first tests on turbojet engines [6], that an inlet distortion reduces pressure ratio and increases the stall mass flow rate, limiting the performance of the engine. Distortion tests have been historically performed using distortion grids of various porosities and angular extensions to be mounted in front of the compressor [7]. Pressure measurements were performed to characterize the impact of the distortion on the steady performance of the compressors. The first attempts to understand the underlying physics of the flow were focused on the development of small-perturbation theories of inviscid incompressible flow [8,9]. From these first theories and experiments it already was clear that work transferred to the flow changes in different regions of the distorted sector and thus sufficient spatial resolution measurements need to be achieved to describe such complex flows. Two additional models [10] and [11] were developed in later decades, and introduced some improvements with respect to older models. The second one in particular is the extension of the celebrated model [12] when distortion is present. In more recent years, the development of high computational power resources has allowed to tackle the problem numerically using CFD [13], coping with the need to have high spatial resolution to investigate the complex flow structures in the distorted regions. For distortion studies, the full annulus must be simulated at the expense of an increased computational cost. From an experimental point of view, particle image velocimetry (PIV) has the potential to capture large sections of the flow to investigate complex features in the distorted regions and to provide data which lend themselves to be compared to CFD simulations results. The technique has been applied to turbomachinery since the late 90s and at the beginning of the new century [14] and today is a quite established technology [15,16,17].

In this paper we thus propose an experimental analysis of the flow using both classical pressure measurements and particle image velocimetry (PIV), to identify and confirm the typical flow features associated with an inlet distortion, in particular at the last stable point before the onset of rotating stall; we also propose a comparison with existing models of parallel compressor [18] and Hynes-Greitzer [11] that are usually used to first assess the stall point of the compressor.

2. EXPERIMENTAL SETUP

The experiments reported in this paper have been performed on the low speed axial compressor CME2 operated at Arts et Métiers, Lille. Its main operating and geometrical parameters are listed in table 1. The distortion has been generated through a screen created from a steel perforated plate and installed one hydraulic diameter in front of the compressor. The angular extension of the investigated screen is 120° and the porosity 0.23 [19]. To measure the non-uniform flow field, the compressor has been equipped with eight total pressure rakes mounted in front of the rotor on the whole circumference at equidistant intervals of 45°.

TABLE 1. PARAMETERS OF THE CME2 AXIAL FLOW COMPRESSOR.

Rotational speed	3200	rpm
Design mass flow rate at 3200rpm	5.3	kg/s
Design total to static pressure ratio	1.03	
Rotor blade number	30	
Stator blade number	40	
Casing diameter	550	mm
Rotor axial chord at mid height	58	mm
Rotor stagger angle at mid height	46	°
Rotor tip gap	0.5	mm

Each rake is fitted with five Kiel probes at different radial positions (figure 1). Each rake also has a static pressure port to measure the casing static pressure. The pressure from the rakes has been registered with two 32 channels pressure scanners. Eight static pressure sensors have been flush mounted on the casing downstream of the stator, at the same azimuthal positions of the rakes (figure 1). All pressure measurements are differential with respect to the atmospheric pressure and have been non-dimensionalized with $1/2\rho U^2$.

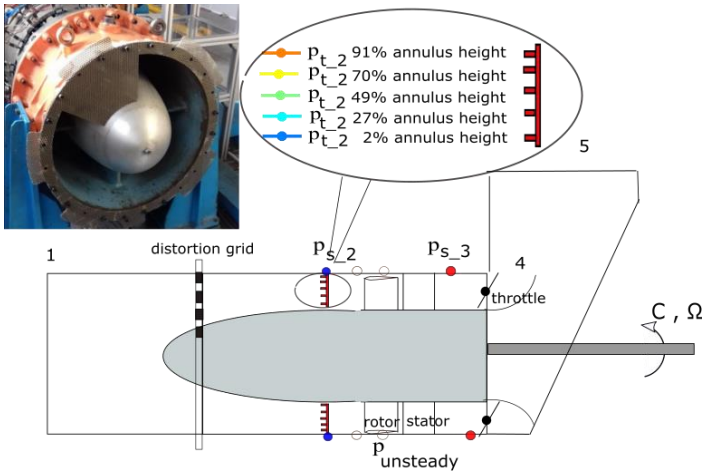

FIGURE 1. SCHEMATIC REPRESENTATION OF THE COMPRESSOR WITH CORRESPONDING PRESSURE MEASUREMENTS POSITIONS; PICTURE OF THE DISTORTION GRID

The full equipment has been used to measure the total to static pressure rise of the compressor. Assuming that the mean flow is axisymmetric, three relative positions of the grid with respect to the rakes have been tested, in order to increase the pressure measurements resolution and to get a total of 24 measurements around the circumference. Unsteady pressure sensors have also been placed to capture the evolution of pressure during the transition towards rotating stall. A first series of six sensors has been placed at -10 mm from the leading edge of the rotor, and a second series of eight probes has been placed at mid chord.
Total pressure measurements have been used for the characterization of the grid. Figure 2 shows the total pressures

behind the grid in nominal flow conditions. The profiles are very similar at different radii so that the distortion can be regarded as purely circumferential. In the following, only the curve obtained at 49% of the channel height will thus be presented. The total pressure loss of the grid non-dimensionalized with $1/2\rho U^2$, is 0.33, and it is thus a significant level of distortion.

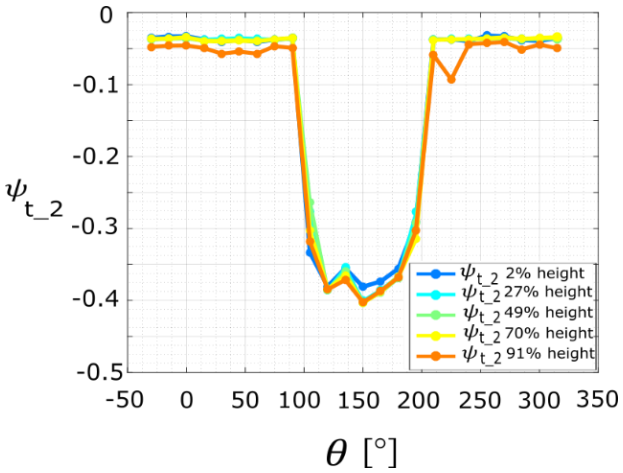

FIGURE 2 TOTAL PRESSURE MEASURED BY THE RAKES; 120° GRID AT NOMINAL MEAN FLOW.

The uncertainty of the instrumentation and of the measured quantities is reported in table 2.

TABLE 2 UNCERTAINTY OF THE INSTRUMENTATION AND/OR OF THE MEASURED QUANTITIES; * ESTIMATED VALUE

	Full scale (FS)	Max error
Total pressure scanners	5 psi	+/- 0.03 % FS
Downstream static pressure sensors	35 kPa	+/- 0.2 % FS
Unsteady pressure probes	6.89 kPa	+/- 0.5 % FS to +/- 1.5% FS
Mass flow rate	18.5 kg/s	+/- 0.5%FS*
Encoder	30000 rpm	+/- 0.3°

In a second experiment, the compressor was equipped to perform endoscopic 2D-2C PIV. The laser is a double cavity Nd:Yag. A mirror arm has been used to guide the laser beam from the laser source to the endoscope (figure 3), which finally guides the laser to the inside of the compressor. At the end of the endoscope, a cylindrical lens generates the laser plane. The flow has been seeded by a smoke generator with droplets of a water-glycol solution. A window on the carter has been used as optical access for the camera, a Lavision sCMOS with a resolution of 2560x2160 px². During a test, the camera was registering 100 pairs of images at around 5 Hz phase locked with the rotor position. After 100 images some particles of smoke were creating a deposit on the window and the quality of the PIV fields was strongly deteriorated. For the post-processing, an in-house multipass algorithm has been used. In the present study, three passes with interrogation windows of 96, 48 and 32 with 50% overlap have been used to compute the mean flow fields. Given the camera resolution and the size of the interrogation windows, it was possible to obtain 2 vectors/mm (109 vectors/pitch, 116 vectors/blade chord).

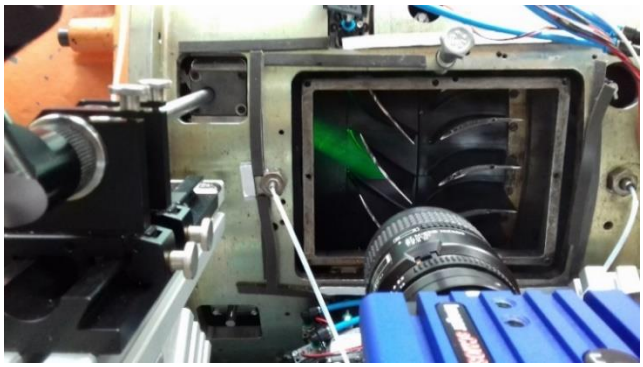

FIGURE 3. PHOTO OF THE COMPRESSOR INSTRUMENTED FOR PIV MEASUREMENTS.

The PIV measurements have been performed on the three radial planes at 79%, 51%, 18% of the blade height and at three positions of the grid (figure 4). The three positions will be referenced with A,B and C in the rest of the text. However, in the present paper, we will focus on the results obtained at 79% of the blade height.

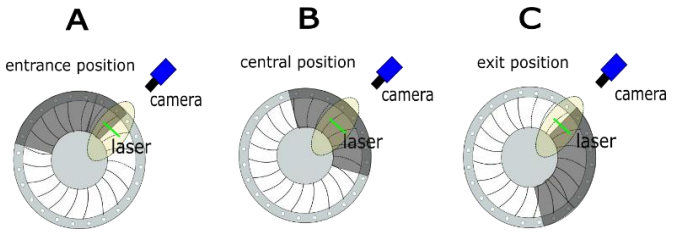

FIGURE 4 SCHEMATIC REPRESENTATION OF THE THREE RELATIVE POSITIONS OF THE GRID WITH RESPECT TO THE LASER PLANE.

3. EXPERIMENTAL RESULTS

In this section, pressure measurements and PIV velocity fields will be presented in order to characterize the distortion generated by the grid in two cases corresponding to the compressor nominal operating point and the last stable point before the onset of the rotating stall. Finally, unsteady pressure measurements will be presented, in order to investigate the effect of the grid stall inception mechanism in comparison with the non-distorted operation.

3.1 Performance at the nominal point

In Figure 5, the curves for the non-distorted operation and the operation with the grid are compared at the nominal flow rate.

The nominal point is at ϕ = 0.52 and it is highlighted in red in figure 5. For this operating flow rate, the local ϕ value has been extracted from PIV fields at 79% height for the three positions of the grid. It has been calculated as the average on an x constant line at 4 mm upstream of the leading edge of the blades in PIV fields (figure 6). The corresponding pressure rise at the three positions of the grid has been extracted from total pressure measurements. Thus, for each ϕ value measured by PIV, the corresponding Ψ measured by pressure sensors is shown in figure 5 with green dots. The flow is such that the blades experience a cycle between these points when they are rotating in and out of the distortion region (qualitatively represented by the dashed line in figure 5).

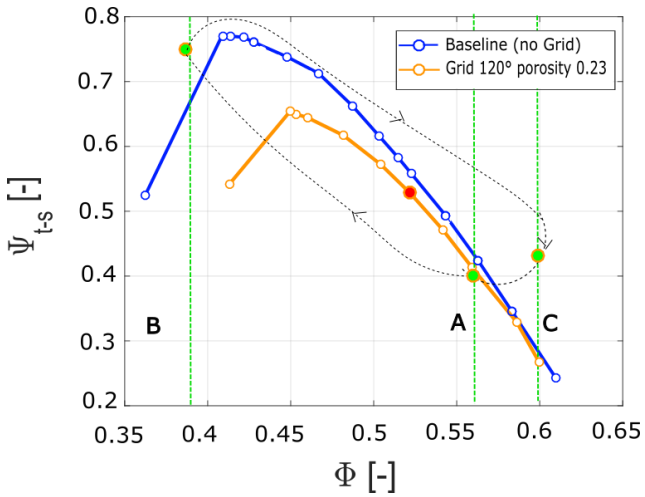

FIGURE 5 CHARACTERISTIC CURVES FOR NON DISTORTED AND DISTORTED OPERATION; RED POINT: MEAN FLOW RATE AT THE NOMINAL POINT; GREEN POINTS: LOCAL FLOW CONDITIONS AT THE ENTRANCE, CENTRE, EXIT OF THE DISTORTION REGION FOR THE SAME MEAN FLOW RATE. CLOCKWISE CYCLE IN DASHED LINE.

The cycle extends to a broad range of ϕ values, due to the high level of distortion. Behind the grid in B, in particular, the flow is at a ϕ which is never encountered in non-distorted operation since it is beyond the stall limit. Figure 7 shows the ϕ values estimated from pressure measurements; first, a ϕ value is calculated from the difference between the total pressure at the rakes and the casing static pressure at the rakes. This calculation assumes that the static pressure at the rakes is constant on the radius, an assumption that can be justified by the low value of tangential component of velocity extracted from PIV fields at different radial positions (figure 6). The error on ϕ (3%) has been estimated using radial equilibrium and considering that the dynamic pressure obtained with the rakes has a component due to the tangential velocity. Then, to evaluate the ϕ at the leading edge from the ϕ evaluated at the rakes, simple conservation of mass has been used to take into account the section variation due to the presence of the convergent hub. The estimated values (figure 7) differ from PIV values especially behind the grid, where the pressure estimated ϕ is lower than the one measured with PIV.

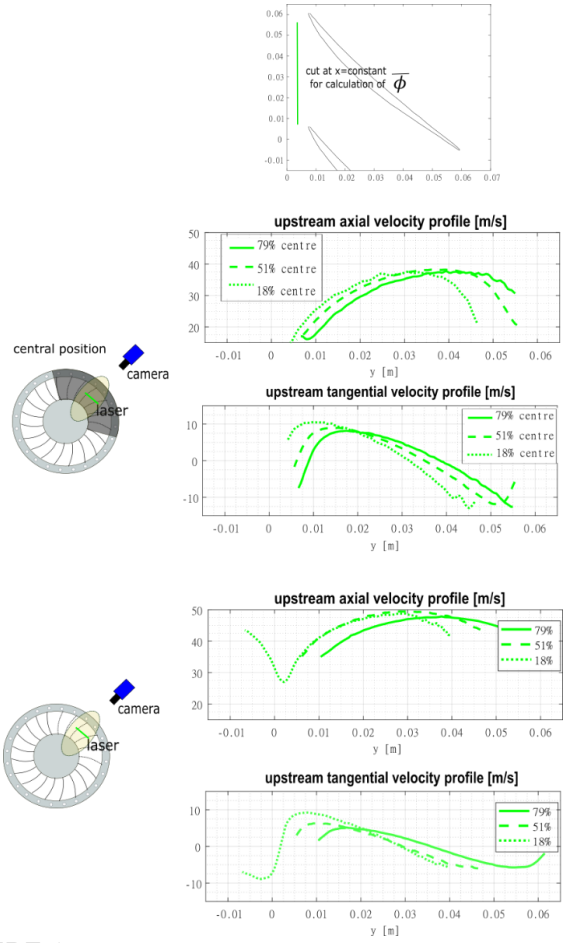

FIGURE 6 AXIAL AND TANGENTIAL COMPONENTS OF THE VELOCITIES EXTRACTED FROM A X CONSTANT CUT IN PIV

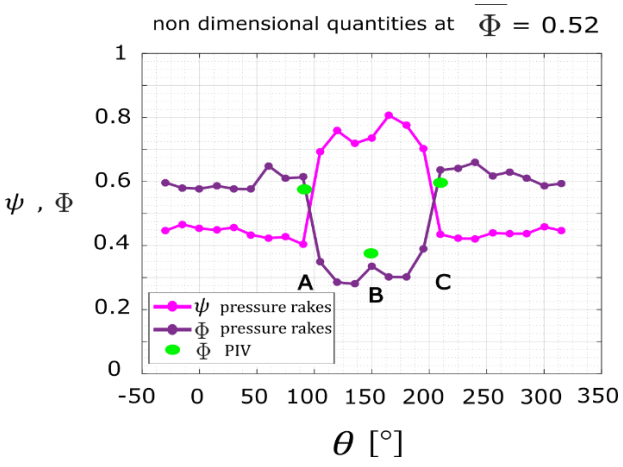

FIGURE 7 PRESSURE COEFFICIENT AND FLUX NUMBER PROFILES MEASURED AS A FUNCTION OF ANGULAR POSITION θ AT NOMINAL MEAN FLOW CONDITIONS

This could be linked to the upstream redistribution effect caused by the compressor, which tends to decrease the velocity distortion [20]. PIV flow fields for the three positions of the grid are shown in figure 8, for the plane at 79% of the blade height; the corresponding velocity triangles are shown in figure 9. They have been calculated averaging the velocities on a constant x cut 4 mm upstream of the leading edge.

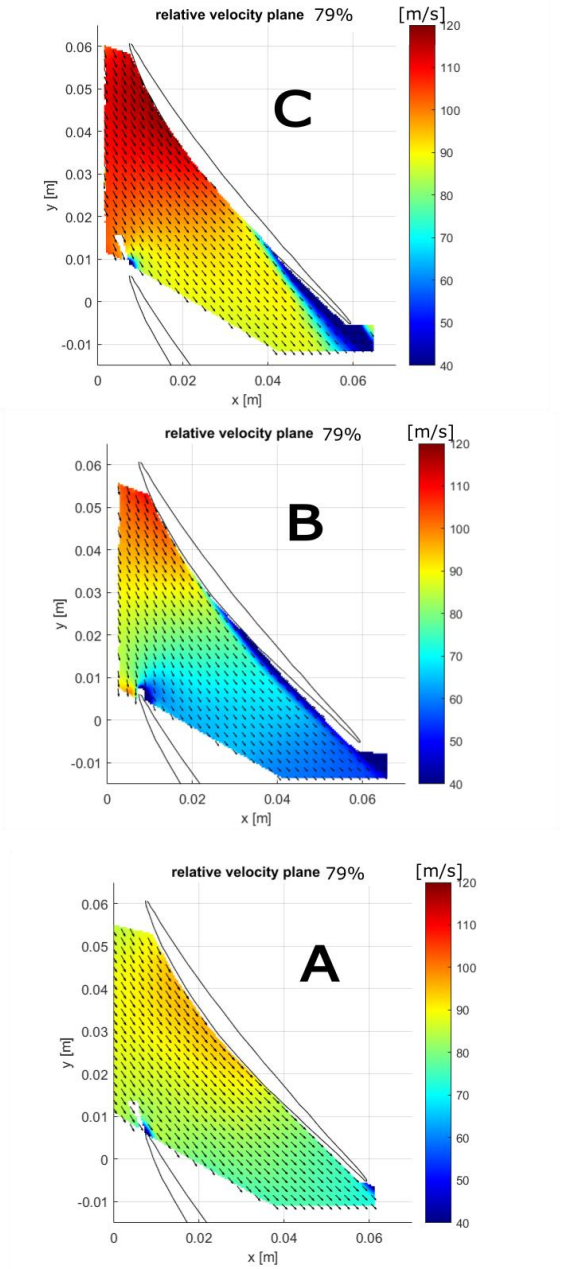

FIGURE 8: PIV-MEASURED RELATIVE VELOCITY FIELDS AT THE EXIT, CENTER AND ENTRANCE OF THE DISTORTION REGION AT NOMINAL MEAN FLOW CONDITIONS.

The three flow fields are very different. In A, at the entrance of the distortion region, the ϕ is higher than nominal and as it can be seen in figure 5, the pressure rise coefficient Ψ is slightly lower than it would be for non-distorted operation at the same ϕ. As it is highlighted by velocity triangles measured from PIV data (figure 9), this is due to a locally reduced incidence on the blades. This reduced local incidence can be explained because of the existence of tangential pressure gradients due to the different pressure regions inside and outside the wake of the grid. These gradients are responsible for redirecting the flow towards the center of the grid thus increasing the incidence in C and decreasing it in A. The field in B presents beginning of separation on the suction surface, but the pressure rise capacity is still preserved even if such a local ϕ would lead to stall in non-distorted conditions. This is consistent with the pressure measurements shown in figure 7 where the point B is still lying on a region of high pressure ratio. In C, at the exit of the distortion region, pressure ratio is higher than it would be in non-distorted conditions. Once again, a contribution to this higher pressure ratio is the tangential pressure gradient at the exit of the distortion region. In fact, this contribution of v_θ to the non-dimensional pressure rise for C can be estimated as:

$$\frac{\rho U v_{\theta 1}}{1/2\,\rho U^2} = \frac{2 v_{\theta 1}}{U} = \frac{2 * 8.7\ m/s}{87\ m/s} = 0.2 \qquad (1)$$

The value is close to the increased pressure rise in figure 5 for the point C. Even if the local ϕ in C is the highest (figure 5), a beginning of separation is present, and even stronger than in B which is at a much lower ϕ.

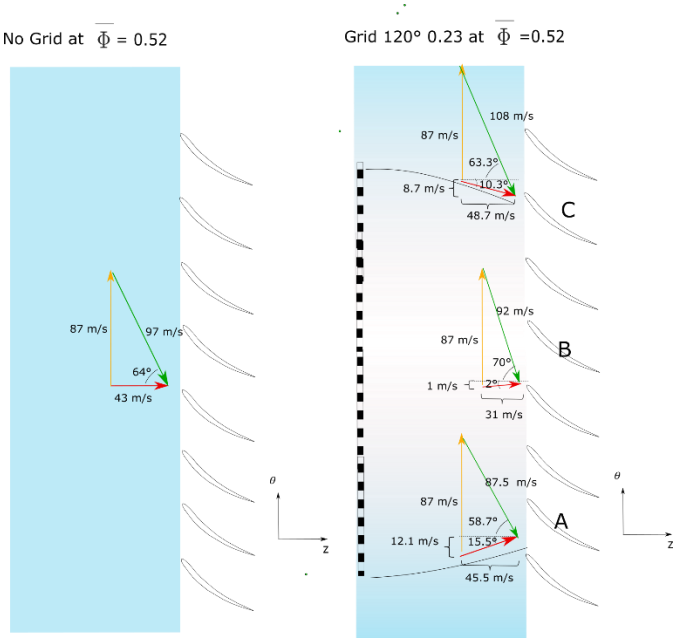

FIGURE 9 VELOCITY TRIANGLES FOR THE NON-DISTORTED CASE AND DISTORTED CASE BOTH AT NOMINAL MEAN FLOW RATE AT 79% BLADE HEIGHT

This can be attributed to flow inertia, since the blades entering the distortion region experience the effect of the increased

incidence of the region B with some time delay, thus towards C at the exit of the distortion region.

3.2 Performance at the last stable point

In figure 10, the curves for non-distorted operation and the operation with the grid at the last stable point before the onset of the rotating stall are compared. The last stable point is at ϕ = 0.45 and is highlighted in red in the figure 10. In figure 11, the pressure profiles for the last stable point are represented. In the same figure the ϕ is also shown, estimated the same way as it was done for the nominal point. Once again its value estimated from pressure is lower than actually measured by PIV.

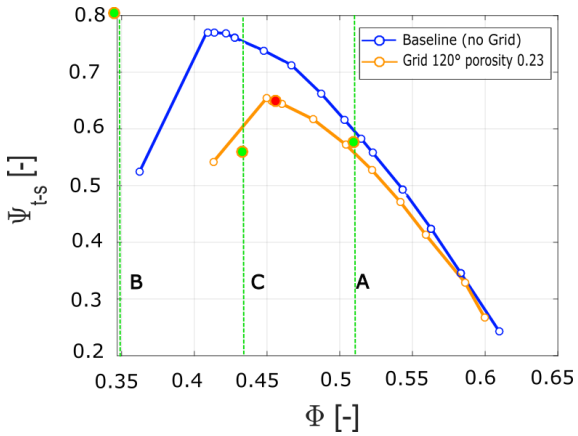

FIGURE 10 CHARACTERISTIC CURVES FOR NON DISTORTED AND DISTORTED OPERATION; RED POINT: MEAN FLOW RATE AT THE LAST STABLE POINT; GREEN POINTS: LOCAL FLOW CONDITIONS AT THE ENTRANCE, CENTRE AND EXIT OF THE DISTORTION REGION FOR THE SAME MEAN FLOW RATE

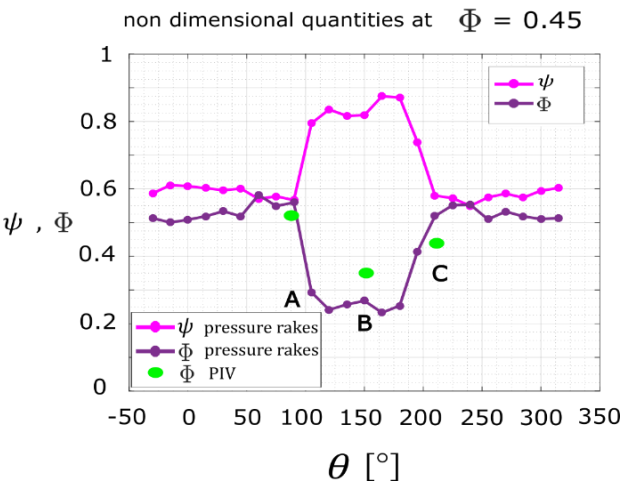

FIGURE 11 PRESSURE COEFFICIENT AND FLUX NUMBER PROFILES MEASURED AS A FUNCTION OF ANGLE θ AT THE LAST STABLE POINT MEAN FLOW CONDITIONS

The pressure rise at the corresponding positions of the grid has been associated to the green points in figure 10. As for the nominal flow rate, the blades are moving through very different flow conditions, with a region in B at a very low flow coefficient, where the compressor would be in stall condition in non-distorted conditions. The PIV fields at the three positions of the grid are shown in figure 12 and the velocity triangles in figure 13. In A the compressor works locally at a higher than average mass flow rate, close to nominal point, both in terms of ϕ and Ψ. The point in B experiences a very low ϕ but still a very high Ψ.

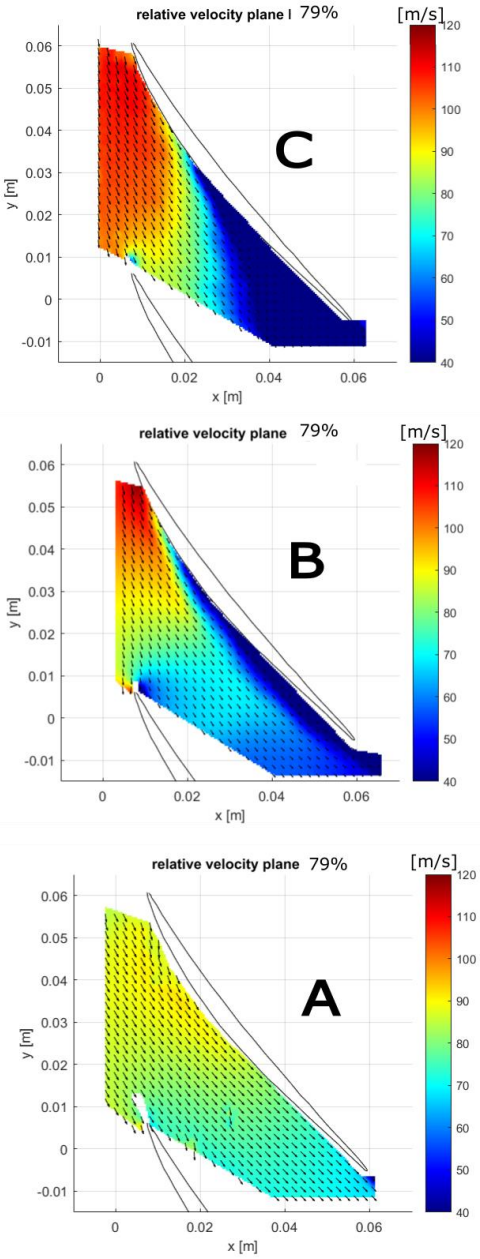

FIGURE 12 PIV MEASURED RELATIVE VELOCITY FIELDS AT THE EXIT, CENTER, ENTRANCE OF THE DISTORTION REGION AT THE LAST STABLE POINT MEAN FLOW CONDITIONS.

Even if the flux number ϕ is so low that the compressor would be in stall in normal non-distorted operation, the loading capacity is partially preserved; just a separation on the suction surface is partially blocking the channel. In C the flow strongly separates, blocking the blade channel; the local ϕ is lower than in A and the low Ψ reflects the loss of loading due to the separation. Once again, to explain the difference between B and C, the effects of the increased incidence in B are felt with time delay in C and unsteady component of work is preventing the flow to separate in B.

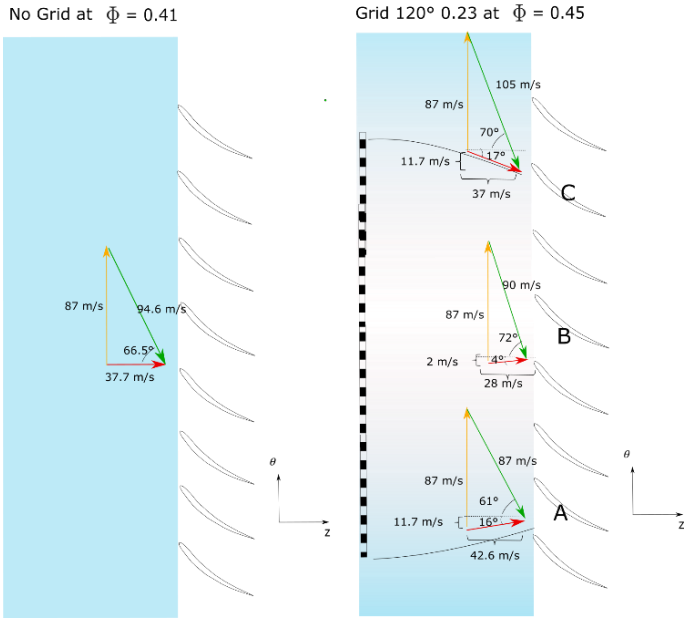

FIGURE 13 VELOCITY TRIANGLES FOR THE NON-DISTORTED CASE AND DISTORTED CASE BOTH AT THE LAST STABLE POINT MEAN FLOW RATE AT 79% BLADE HEIGHT.

3.3 Rotating stall inception

A series of unsteady pressure probes flush mounted on the casing have been used to track the evolution of rotating stall. In normal uniform flow operation, the compressor stall is of spike type [21]. An example of a usual stall transition in non-distorted operation is shown in figure 14. A first spike propagating and increasing in amplitude leading to the formation of rotating stall cells is clearly visible. On the same figures are represented the positions of the unsteady pressure probes on the two rings of the circumference. In figure 15, a transition towards rotating stall for the case with the grid is represented instead. In figure 16 the same transient is represented on a more limited number of revolutions. It is still possible to recognize a spike in the first three signals between 0 and 180° (figure 16), but some modal oscillations are appearing in the signals around 10-20 revolutions before rotating stall, especially in the signals between 180° and 325°, which are originated outside the region of flow occupied by the grid, towards the exit of the distortion region. These features suggest a competition of modal and spike types rotating stall.

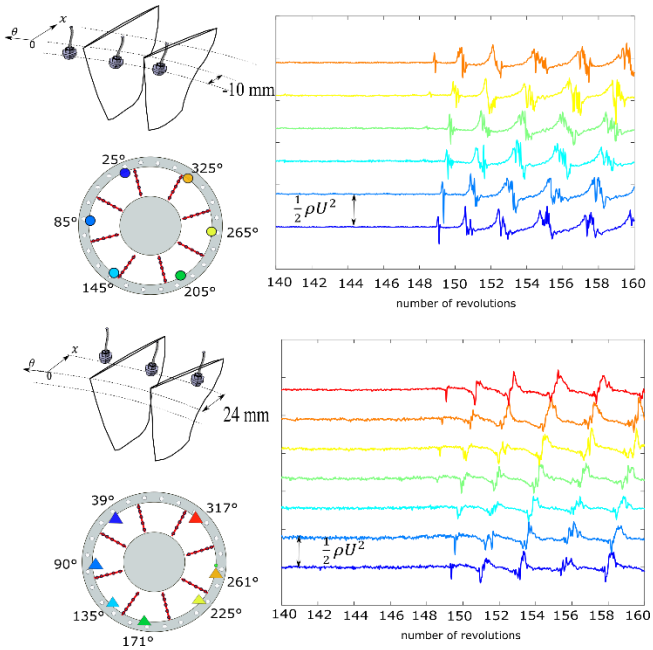

FIGURE 14 SPIKE TYPE ROTATING STALL INCEPTION IN NON-DISTORTED OPERATION

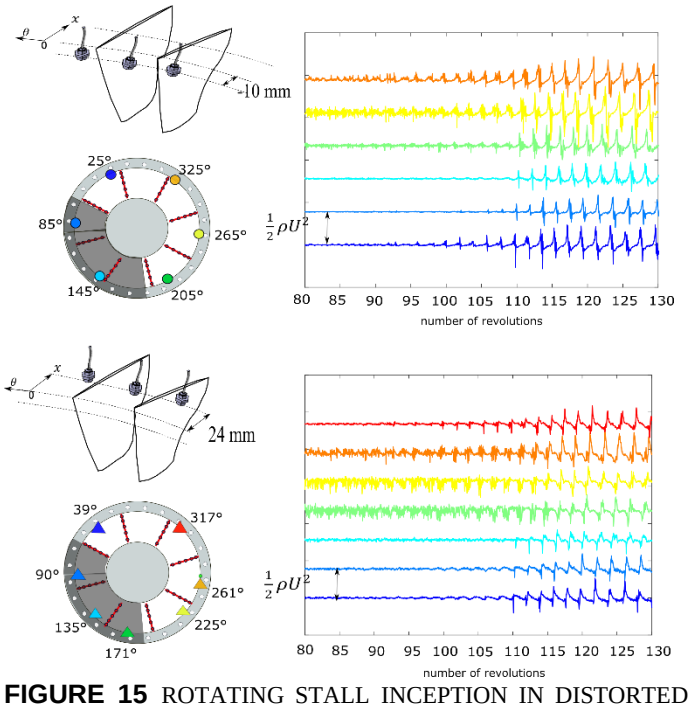

FIGURE 15 ROTATING STALL INCEPTION IN DISTORTED OPERATION WITH THE 120° GRID

A Fourier analysis (figure 17) on the signals prior to the development of rotating stall (from 1 to 60 revolutions) indicates that indeed a mode is present in all the signals at a frequency of 28.23 Hz, corresponding to 53% of the rotor frequency.

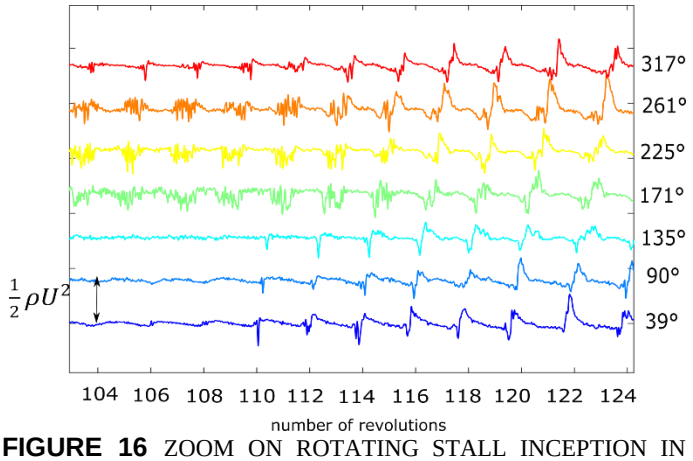

FIGURE 16 ZOOM ON ROTATING STALL INCEPTION IN DISTORTED OPERATION WITH THE 120° GRID; MID-CHORD MEASUREMENTS

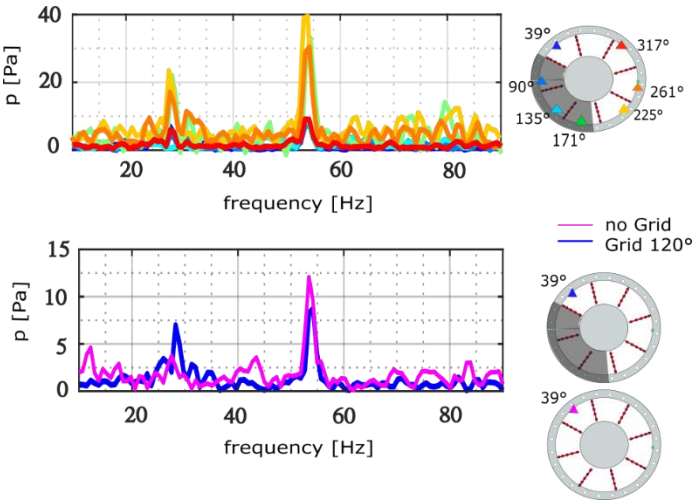

FIGURE 17 TOP: FOURIER AMPLITUDES OF THE SIGNALS IN FIGURE 16 BETWEEN THE 1ST AND THE 60TH REVOLUTION; BOTTOM: COMPARISON BETWEEN DISTORTED (GRID 120°) AND NON-DISTORTED SIGNAL (NO GRID).

This frequency corresponds to the propagating speed of the perturbations clearly visible in the signals of figure 16 before the arise of rotating stall at the 112th revolution. Even for the signals in between 0° and 180°, the same frequency is captured by the Fourier analysis, even if the amplitude is lower, coherently with the fact that the oscillations are not standing out of the signals as clearly as in the region between 180° and 325°. This suggests that rotating stall cells are already forming and developing before the occurrence of the spike at the 110th revolution but they are damped when passing behind the grid. The interpretation of these perturbations before the 110th revolution as forming rotating stall cells could be supported by the fact that their frequency is close to the frequency of developed rotating stall cells. In fact, if a Fourier analysis is performed on the portion of the signals in developed stall (from 130 revolutions onwards), the dominating mode has frequency 25.94 Hz corresponding to 48.6% of the rotor frequency i.e the propagation speed of rotating stall cells.

4. COMPARISON WITH MODELS AND INTERPRETATION

The experimental distorted characteristic curve has been compared to numerical models existing in literature: the parallel compressor as formulated in [18], the Hynes and Greitzer model, [11] for the steady state distorted performance and Lin's model [22] for the prediction of the instability onset. The parallel compressor model [18] states that the overall compressor performance is the average of two compressors working at two different operating points, one in the undistorted region developing the same pressure ratio as in uniform flow, and one in the distorted region developing a higher pressure ratio closer to the stall limit. The overall compressor stalling point is assumed to be reached when the pressure rise of the sub-compressor in the distorted region equals the stalling pressure rise in usual non distorted operation. The model of Hynes and Greitzer rather computes the local flux number as resulting from a compressor characteristic-circuit equilibrium equations as reported below (2).

$$\begin{cases} \dfrac{p_3 - p_{t2}(\theta)}{\rho U^2} = \psi(\phi_2) - \lambda \dfrac{d\phi_2}{d\theta} \\ \dfrac{p_3 - p_5}{\rho U^2} = \dfrac{T}{2}\overline{\phi_2}^{-2} \end{cases} \qquad (2)$$

The ψ in the equations is the experimental non-distorted steady characteristic curve and it has been fitted with a cubic polynomial to be an input to the model. Another key input parameter is λ. It is a geometrical parameter associated to fluid inertia obtained from time scale considerations [23], and it controls the lag in the pressure response due to an acceleration of the flow in the blade passage. In our compressor it takes the value

$$\lambda = \frac{b_x}{r\ (\cos\gamma)^2} = \frac{0.0584\ m}{0.2415\ m * (\cos 46°)^2} = 0.5 \qquad (3)$$

Lin's model is a high order extension of the Moore Greitzer model [11] with the presence of inlet distortion, and it introduces all the system dynamics to calculate the actual rotating stall transient. For the system of equations see directly [22].
In figure 18 we studied the sensitivity of Lin's model to the model parameter λ and we show that upon an increase of λ, hence of the model inertia, the system instability onset gets shifted towards lower flow rates (see magenta open markers). Considering the correct parameter λ, corresponding to our compressor (λ =0.5) provides a remarkably good predictive result of the critical flow rate parameter $\bar{\phi}$.

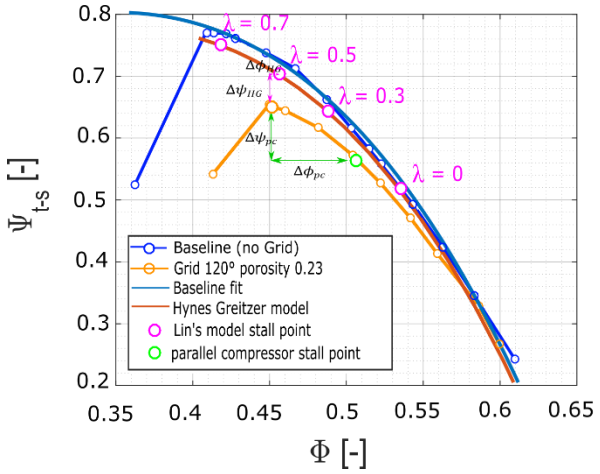

FIGURE 18 COMPARISON BETWEEN EXPERIMENTAL CURVE AND HYNES GREITZER CURVE. LIN'S MODEL LAST STABLE POINT HIGHLIGHTED FOR DIFFERENT VALUES OF THE PARAMETER λ (MAGENTA), PARALLEL COMPRESSOR LAST STABLE POINT HIGHLIGHTED IN GREEN

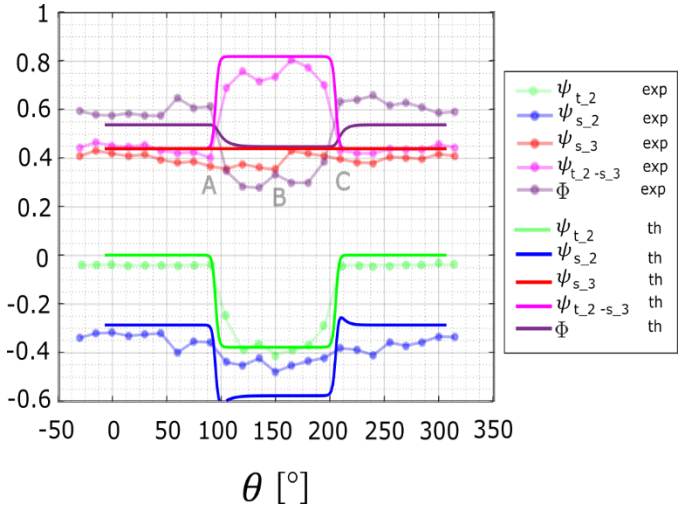

FIGURE 19 COMPARISON BETWEEN EXPERIMENTAL (EXP) AND HYNES GREITZER (TH) PRESSURE PROFILES FOR A $\bar{\Phi} = 0.52$

On the other hand, the pressure rise coefficient is overpredicted by the model of Hynes Greitzer, as also reported in literature [1]. For λ=0 the model approaches the hypothesis of the parallel compressor approach, even though the latter includes further simplifications; the major difference between the parallel compressor and Hynes and Greitzer consists of the treatment of the grid-induced pressure drop term. The model of Hynes and Greitzer deals with it as fully-nonlinear term, while the parallel compressor assumes that the pressure drop can be modelled as a square wave. This leads to the minor differences observed between the magenta open markers for λ =0 and the green open marker (compressor in parallel). As also reported in literature [24], the parallel compressor approach strongly overestimates the critical flow rate coefficient. By comparison between the two models, we infer that a major role in the prediction of the instability onset is played by inertia rather than nonlinear interaction with the pressure drop, which is consistent with the poor prediction of the inertia-less parallel compressor approach. In figure 19 are compared the measured and numerical pressure and velocity profiles for the nominal point. The estimated amplitude of the ϕ is lower than in the experiments and correspondingly the static pressure amplitude is higher. In the model thus, the velocity distortion is underestimated and so the loss of pressure ratio.

5. CONCLUSIONS

Pressure and PIV measurements have been performed in an axial flow compressor operated with inlet flow distortion. Experimental compressor characteristic curve and pressure profiles on the circumference have also been compared to numerical model calculated curves. From PIV fields it is evident the flow inertia which is responsible for allowing the distorted region of flow to operate at local flow rates well beyond the usual non-distorted limit. This is consistent with the bad prediction of the parallel compressor and with the remarkably good one of Lin's model which takes into account the inertial effect of the flow. This agreement in particular is remarkable, as the delay in response is for sure influenced also by separation and secondary flows as they appear in PIV fields, but even a simpler representation of the blade passage dynamics with the λ parameter is able to capture the flow coefficient of the stall limit for a high distortion level. The PIV also clearly shows an angle distortion due to the pressure gradients generated by the upstream redistribution of the flow in front of the rotor. This angle distortion is responsible for modifying the velocity triangles on the sides of the distorted region and thus local work done on the flow. In the model of Hynes and Greitzer this upstream redistribution effects are not modelled, which contribute to explain the difference between the experimental and the numerical characteristic curves. Unsteady pressure measurements also indicate an effect of the grid on the onset of rotating stall, since some modal oscillations appear before the apparition of the first spike, suggesting a concurrency of spike and modal type of stall.

ACKNOWLEDGEMENTS

The work is supported by DGAC (the French Agency For Civil Aviation) through the SUBLIME research program. A special acknowledgement is dedicated to Christophe Cuvier (University lecturer at Centrale Lille) and Jean Claude Monnier (Research Engineer at ONERA Lille) for their support for the PIV experimental campaign.

REFERENCES

[1] Fidalgo, V. Jerez, C. A. Hall, and Y. Colin. 2012. “A Study of Fan-Distortion Interaction Within the NASA Rotor 67 Transonic Stage.” *Journal of Turbomachinery* 134 (5).

[2]Stephens, J.E., Celestina, M. and Hughes C. 2019. “Swirl Distortion Using Stream Vanes for Boundary Layer Ingestion Research.” In *Proceedings of the ASME Turbo Expo 2019: Turbomachinery Technical Conference and Exposition. Phoenix, Arizona, USA.*

[3] Guimarães Tamara, Lowe Kevin T, O'Brien Walter F. 2019 “Vortical Flow Development in Round Ducts across Scales for Engine Inlet Applications” *Experiments in Fluids,* 60, 52.

[4] MacManus D.G., Chiereghin N., Gil Prieto D., Zachos P.K. 2017. “Complex Aeroengine Intake Ducts and Dynamic Distortion .” *AIAA* , 55(7).

[5] Hall, David K., Arthur C. Huang, Alejandra Uranga, Edward M. Greitzer, Mark Drela, and Sho Sato. 2017. “Boundary Layer Ingestion Propulsion Benefit for Transport Aircraft.” *Journal of Propulsion and Power*, March

[6] Conrad, E. William, and Adam E. Sobolewski. 1950. “Investigation of Effects of Inlet-Air Velocity Distortion on Performance of Turbojet Engine.” Report. UNT Digital Library. September 13, 1950.

[7] Reid, C. 1969. “The Response of Axial Flow Compressors to Intake Flow Distortion.” In *ASME*. Derby, England.

[8] Rannie, W. Duncan, and Frank E. Marble. 1957. “Unsteady Flows in Axial Turbomachines.” Report or Paper. Caltech. 1957.

[9] Katz, Robert. 1958. “Performance of Axial Compressors with Asymmetric Inlet Flows.” Report or Paper. Pasadena, CA: California Institute of Technology. June 1958.

[10]Mazzawy, R. S. 1977. “Multiple Segment Parallel Compressor Model for Circumferential Flow Distortion.” *Journal of Engineering for Power* 99 (2): 288–96.

[11] Hynes, T. P., and E. M. Greitzer. 1987. “A Method for Assessing Effects of Circumferential Flow Distortion on Compressor Stability.” *Journal of Turbomachinery* 109

[12] Moore, F. K., and E. M. Greitzer. 1986. “A Theory of Post-Stall Transients in Axial Compression Systems: Part I—Development of Equations.” *Journal of Engineering for Gas Turbines and Power* 108 (1): 68–76.

[13] Lesser, Andreas, and Reinhard Niehuis. 2014. “Transonic Axial Compressors With Total Pressure Inlet Flow Field Distortions.” In . American Society of Mechanical Engineers Digital Collection.

[14] Balzani, N., F. Scarano, M. L. Riethmuller, and F. A. E. Breugelmans. 2000. “Experimental Investigation of the Blade-to-Blade Flow in a Compressor Rotor by Digital Particle Image Velocimetry.” *Journal of Turbomachinery* 122 (4): 743–50.

[15] Guimarães Tamara B., Lowe Kevin T., Nelson Michael, O'Brien Walter F., Kirk Caroline. 2015. “Stereoscopic PIV measurements in a turbofan engine inlet with tailored swirl distortion” In *31st AIAA Aerodynamic Measurement Technology and Ground Testing Conference* American Institute of Aeronautics and Astronautics.

[16] Voges M., Willert C., Mönig R., Schiffer H.P. “The Effect of a bend-slot Casing Treatement on the Blade Tip Flow Field of a Transonic Compressor Rotor” In *Proceedings of ASME Turbo Expo 2013: Turbine Technical Conference and Exposition*

[17] Migliorini Matteo, Zachos Pavlos K., MacManus David G. 2019 “An Assessment of the Unsteady Flow Distortion Generated by an S-duct Intake” *AIAA Propulsion and Energy 2019 Forum*

[18] Braitwhaite, W., JR. E. Graber, and C. Mehalic. n.d. “The Effect of Inlet Temperature and Pressure Distortion on Turbojet Performance.” In *9th Propulsion Conference*. American Institute of Aeronautics and Astronautics. Accessed November 28, 2021

[19] Baretter Alberto, Benjamin Godard, Pierric Joseph, Olivier Roussette, Francesco Romanò, Raphael Barrier, and Antoine Dazin. 2021. “Experimental and Numerical Analysis of a Compressor Stage under Flow Distortion.” *Int. J. Turbomach, Propuls, power, 6(4),43*

[20] Pearson, H., and A. B. McKenzie. 1959. “Wakes in Axial Compressors.” *The Aeronautical Journal* 63 (583)

[21] Margalida, Gabriel, Pierric Joseph, Olivier Roussette and Antoine Dazin. 2021. “Active flow control in an axial compressor for stability improvement: on the effect of flow control on stall inception.” *Experiments in Fluids,* 62(1): 12.

[22] Lin, Peng, Cong Wang, and Yong Wang. 2017. “A High-Order Model of Rotating Stall in Axial Compressors with Inlet Distortion.” *Chinese Journal of Aeronautics* 30 (3):

[23] Moore, F. K. 1984. “A Theory of Rotating Stall of Multistage Axial Compressors: Part I—Small Disturbances.” *Journal of Engineering for Gas Turbines and Power*

[24] Chue, R., T. P. Hynes, E. M. Greitzer, C. S. Tan, and J. P. Longley. 1989. “Calculations of Inlet Distortion Induced Compressor Flow Field Instability.” *International Journal of Heat and Fluid Flow* 10 (3): 2